Maximizing temporal quantum correlation by approaching an exceptional point

Chun-Wang Wu,[1,2,3,*] Man-Chao Zhang,[1,2,3,*] Yan-Li Zhou,[1,2,3] Ting Chen,[1,2,3] Ran Huang,[4] Yi Xie,[1,2,3] Bao-Quan Ou,[1,2,3] Wei Wu,[1,2,3] Adam Miranowicz,[5] Jie Zhang,[1,2,3,†] Hui Jing,[4,‡] and Ping-Xing Chen[1,2,3,§]

[1]*Institute for Quantum Science and Technology, College of Science, NUDT, Changsha 410073, Hunan, China*
[2]*Hunan Key Laboratory of Quantum Information Mechanism and Technology, NUDT, Changsha 410073, Hunan, China*
[3]*Hefei National Laboratory, Hefei 230088, Anhui, China*
[4]*Department of Physics and Synergetic Innovation Center for Quantum Effects and Applications, Hunan Normal University, Changsha, China*
[5]*Institute of Spintronics and Quantum Information, Faculty of Physics, Adam Mickiewicz University, 61-614 Poznań, Poland*

(Dated: April 14, 2023)

Quantum correlations, both spatial [1] and temporal [2], are the central pillars of quantum mechanics. Over the last two decades, a big breakthrough in quantum physics is its complex extension to the non-Hermitian realm, and dizzying varieties of novel phenomena and applications beyond the Hermitian framework have been uncovered [3, 4]. However, unique features of non-Hermitian quantum correlations, especially in the time domain, still remain to be explored. Here, for the first time, we experimentally achieve this goal by using a parity-time ($\mathcal{PT}$)-symmetric trapped-ion system. The upper limit of temporal quantum correlations, known as the algebraic bound, which has so far not been achieved in the standard measurement scenario, is reached here by approaching the exceptional point (EP), thus showing the unexpected ability of EPs in tuning temporal quantum correlation effects. Our study, unveiling the fundamental interplay of non-Hermiticity, nonlinearity, and temporal quantum correlations, provides the first step towards exploring and utilizing various non-Hermitian temporal quantum effects by operating a wide range of EP devices, which are important for both fundamental studies and applications of quantum EP systems.

Quantum correlations, as the cornerstones of quantum mechanics, have played an essential role in the emerging field of quantum information science and technology [5, 6]. Among them, quantum correlations between spatially separated systems, referred as spatial quantum correlations, can be benchmarked by the famous Bell inequalities [1]. Likewise, those between temporally separated states of a single system, referred as temporal quantum correlations, can be benchmarked by the Leggett-Garg inequalities, usually termed as temporal Bell inequalities [2]. Recently, temporal quantum correlations have attracted widespread interests because of their unique applications in harnessing long-lived quantum coherence in biological systems [7–9], discriminating quantum transport [10, 11], witnessing non-Markovianity [12], and supplying the beyond-classical power of quantum computation [13, 14], to name only a few. In principle, there is an upper limit of temporal quantum correlations, known as the algebraic bound, but in practice it remains a challenge for conventional Hermitian quantum systems to reach this limit; instead, in the standard measurement scenario, only half of this limit, known as the Lüders bound, has been achieved till now [15–26]. Hence, this hinders the deep understanding and further utilizations of temporal quantum effects beyond the Lüders bound.

We also note that, despite extensive studies of non-Hermitian effects and their unique applications in a wide range of systems, the experimental observation of temporal quantum correlations has not been realized till now. To fill this gap, here, we experimentally study the temporal quantum correlations of a non-Hermitian parity-time ($\mathcal{PT}$)-symmetric qubit, realized as a submanifold of a high-dimensional trapped-ion system. We show that the accelerated dynamics, induced by nonlinear properties of this system, can induce enhanced temporal quantum correlations beyond the Lüders bound (FIG. 1a). Especially, by approaching an exceptional point (EP), the upper limit of the temporal correlations in the standard measurement scenario is, for the first time ever, achieved by this work. We further measure the value of the quantum witness, another indicator of temporal quantum correlations, which can also break the upper bound for the Hermitian case. Our work promotes the experimental study of quantum correlations beyond the Hermitian realm, and also demonstrates new facets of non-Hermitian systems from the viewpoint of temporal correlations, enabling a deeper understanding and a better control of this peculiar but utilitarian type of open systems.

Temporal quantum correlations can be quantified by the violation extent of the temporal Bell inequality, that Leggett and Garg proposed in 1985 for the original purpose of detecting macroscopic coherence [2]. For a dichotomic observable $Q = \pm 1$, the temporal Bell inequality reads

$$K_3 = C_{12} + C_{23} - C_{13} \leqslant 1, \tag{1}$$

* These authors contributed equally to this paper.
† Corresponding author: zj1589233@126.com
‡ Corresponding author: jinghui73@foxmail.com
§ Corresponding author: pxchen@nudt.edu.cn

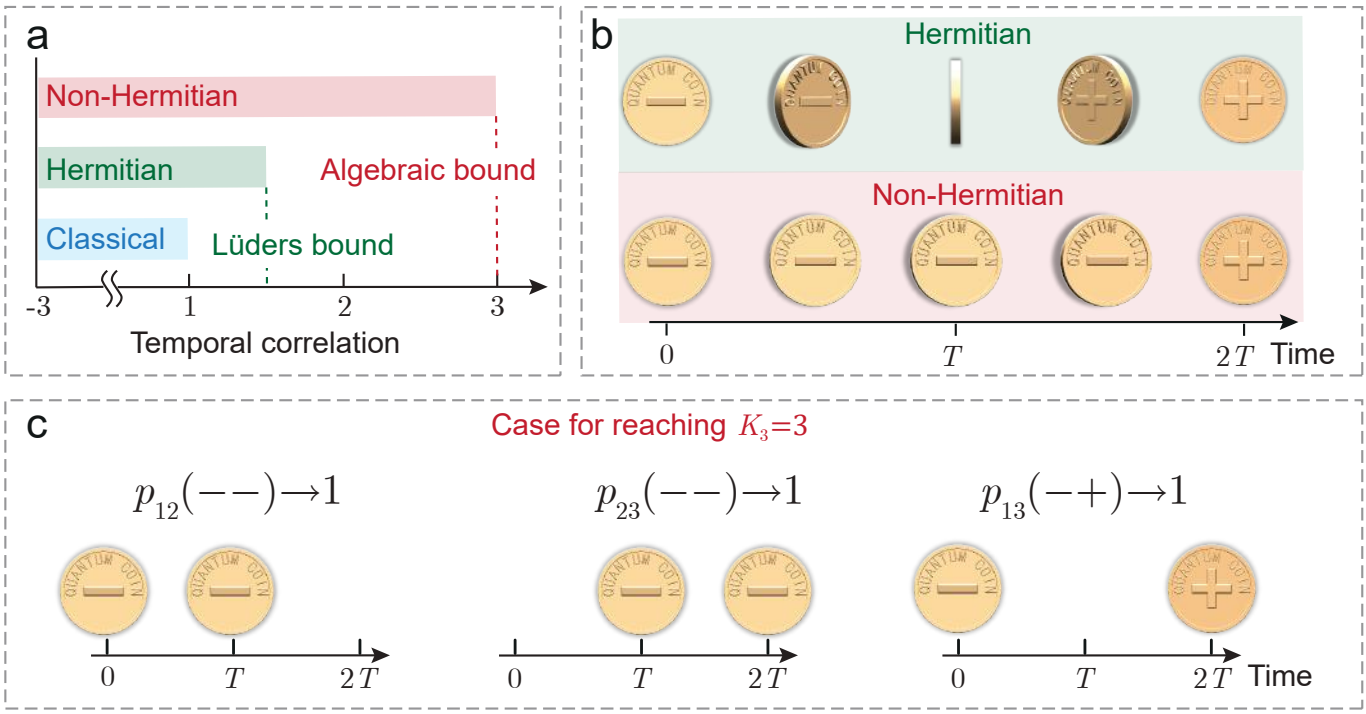

FIG. 1. **Allowed ranges of temporal quantum correlations for different types of physical systems, and the enhancement mechanism of temporal correlations by non-Hermiticity. a**, The temporal quantum correlations for classical, Hermitian quantum, and non-Hermitian quantum systems are bounded by 1, the Lüders bound ($K_3 = 1.5$), and the algebraic bound ($K_3 = 3$), respectively. **b**, A Hermitian quantum coin flips coherently from $|-\rangle$ to $|+\rangle$ with a uniform speed in a time period $[0, 2T]$. However, a non-Hermitian quantum coin can finish the same flip with an extremely nonuniform flip speed, which is infinitesimal for times not close to the moment $2T$, but infinitely great in the neighborhood of $2T$. **c**, Successive measurements performed in pairs of time on the non-Hermitian flip dynamics give a counterintuitive combination of the joint probabilities for measurement outcomes, resulting in the algebraic bound of the temporal quantum correlations $K_3 = 3$.

where $C_{ij} = \langle Q(t_i)Q(t_j)\rangle$ is the two-time correlation function at times t_i and t_j. The allowed ranges of the Leggett-Garg parameter K_3 for classical, Hermitian, and non-Hermitian quantum systems are shown in FIG. 1a. It should be noted that, in the Hermitian quantum case, K_3 beyond the Lüders bound can be observed by devising delicate modifications to the standard Leggett-Garg test scenario, such as introducing multi-time correlation functions [27], or using multi-projector measurements [28–32]. Here, in the framework of the standard test scenario, we focus on the non-Hermitian enhancement of the temporal quantum correlations.

The enhancement mechanism of temporal quantum correlations due to non-Hermiticity can be illustrated by comparing the Hermitian and non-Hermitian dynamics [33, 34] [FIG. 1(b, c)]. Suppose we have a quantum coin, which can be in the superposition state $|\psi\rangle = \cos\left(\frac{\delta}{2}\right)|-\rangle + \sin\left(\frac{\delta}{2}\right)|+\rangle$, and the measurement will make it collapse to $|-\rangle$, $|+\rangle$ with probabilities $p_- = \cos^2(\frac{\delta}{2})$, $p_+ = \sin^2(\frac{\delta}{2})$, meanwhile obtaining the observed values $Q = -1$, $Q = +1$, respectively. In the Hermitian case, without measurement, the coin flips coherently from $|-\rangle$ to $|+\rangle$ with a uniform speed in a time period $[0, 2T]$ (FIG. 1b). However, in the non-Hermitian case, the coin can finish the same flip with an extremely nonuniform speed, which is infinitesimal in most of the times $t < 2T$ but infinitely great in the neighborhood of $2T$. A measurement performed at the time $t < 2T$ on the non-Hermitian coin will destroy the little coherence accumulated and collapses the quantum state to $|-\rangle$ with a probability close to 1, leading to a reset of the quantum flip process to the start. To implement the Leggett-Garg test, we choose $t_1 = 0$, $t_2 = T$, and $t_3 = 2T$, and define $p_{ij}(Q_i, Q_j)$ as the joint probability for the outcomes Q_i, Q_j of quantum measurements performed at times t_i and t_j, respectively. Then, successive measurements performed in pairs on the non-Hermitian flip dynamics give $p_{12}(-,-) \sim 1$, $p_{23}(-,-) \sim 1$, and $p_{13}(-,+) \sim 1$, resulting in the maximal temporal quantum correlation corresponding to $K_3 = 3$ (FIG. 1c). The acceleration dynamics of the non-Hermitian quantum coin imply that its evolution speed is extremely sensitive to the parameter δ, which is a behavior easy to appear in nonlinear dynamics.

The quantum nonlinear properties donot appear in general Hermitian systems, but may be found in non-Hermitian systems. Consider a simple non-Hermitian system, which consists of two quantum energy levels

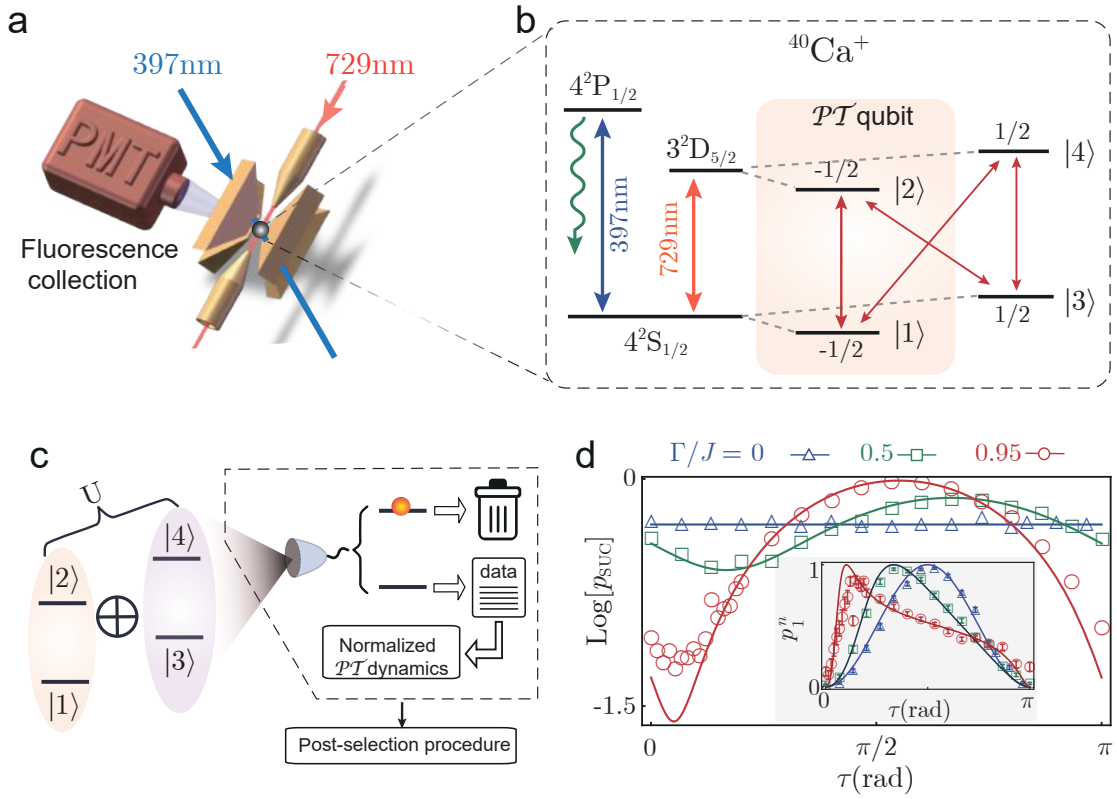

FIG. 2. **Experimental overview. a**, **b**, Our experiment uses Zeeman sublevels in $S_{1/2}$ and $D_{5/2}$ manifolds of a single $^{40}Ca^+$ ion, trapped in a linear Paul trap, to construct a 4-dimensional Hilbert space embedding the parity-time ($\mathcal{PT}$)-symmetric qubit. The narrow-linewidth laser at 729 nm can be used to realize equatorial rotations on any $S-D$ transition. The state-dependent fluorescence, observed using a photo-multiplier (PMT), while driving $S_{1/2}-P_{1/2}$ transition with 397 nm laser, is used for the post-selection procedure. **c**, The normalized $\mathcal{PT}$ dynamics is realized via enforcing a unitary operation U on the directed sum space $\mathcal{H}_S \bigoplus \mathcal{H}_A$, with $\mathcal{H}_S$ and $\mathcal{H}_A$ expanded by $\{|1\rangle, |2\rangle\}$ and $\{|3\rangle, |4\rangle\}$ respectively, followed by a post-selection procedure which discards the cases where $\mathcal{H}_A$ is occupied. **d, e**, The post-selection probability $p_{\rm suc}$, and the normalized population of the state $|1\rangle$, denoted as p_1^n, are measured versus the scaled time τ for various values of Γ/J, which verify the quantum power oscillation phenomenon in the unbroken $\mathcal{PT}$-symmetry zone and the nonlinear dynamics of Eq. (3).

$\{|1\rangle, |2\rangle\}$, coupled with the rate J, and has a balanced gain (on $|1\rangle$) and loss (on $|2\rangle$), with the rate Γ. This system can be described by an effective non-Hermitian Hamiltonian with $\mathcal{PT}$ symmetry

$$\hat{H}_{\rm PT} = J\hat{\sigma}_x + {\rm i}\Gamma\hat{\sigma}_z, \tag{2}$$

where $\hat{\sigma}_x = |1\rangle\langle 2| + |2\rangle\langle 1|$ and $\hat{\sigma}_z = |1\rangle\langle 1| - |2\rangle\langle 2|$ are the Pauli operators, and $\hat{H}_{\rm PT}$ commutes with the parity-time-reversal operator $\hat{\mathcal{P}}\hat{\mathcal{T}}$, i. e. $[\hat{H}_{\rm PT}, \hat{\mathcal{P}}\hat{\mathcal{T}}] = 0$. In the case of $J > \Gamma$, i. e. the $\mathcal{PT}$-symmetric unbroken region (PTS), its time evolution operator $\hat{U}_{\rm PT} = \exp\left(-i\hat{H}_{\rm PT}t\right)$ gives rise to dynamics very similar to the Hermitian case, and the populations of $|1\rangle$ and $|2\rangle$, denoted as p_1 and p_2, will exhibit Rabi-like oscillations with the frequency $\Omega = \sqrt{J^2 - \Gamma^2}$. However, quite unlike the Hermitian case, the total population $p = p_1 + p_2$ also exhibits periodic oscillatory behavior, which can be understood as a quantum version of the power oscillation phenomenon in classical $\mathcal{PT}$-symmetric systems [35]. After normalization, the density operator $\hat{\rho}(t)$ of this system satisfies the nonlinear equation [36]

$$\dot{\hat{\rho}} = -{\rm i}J[\hat{\sigma}_x, \hat{\rho}] + \Gamma\{\hat{\sigma}_z, \hat{\rho}\} \underbrace{-2\Gamma\hat{\rho}[{\rm Tr}(\hat{\sigma}_z\hat{\rho})]}_{\text{the nonlinear term}}. \tag{3}$$

The nonlinear term in Eq. (3) can lead to an uneven speed of flip up and down, which cannot be found in the linear Hermitian dynamics.

In our experiment, the high-dimensional Hilbert space, embedding the $\mathcal{PT}$-symmetric qubit, is realized using a single $^{40}Ca^+$ ion, trapped in a blade-shaped linear Paul trap [FIG. 2(a, b)]. The Zeeman sublevels $S_{1/2}(m_J = -1/2)$, $D_{5/2}(m_J = -1/2)$, $S_{1/2}(m_J = 1/2)$ and $D_{5/2}(m_J = 1/2)$ in a magnetic field of 5.3 G are chosen as quantum states $|1\rangle$, $|2\rangle$, $|3\rangle$, and $|4\rangle$, respectively. The equatorial rotations $R(\theta, \phi) = \exp\left[-{\rm i}\theta(\cos(\phi)\sigma_x^m + \sin(\phi)\sigma_y^m)/2\right]$ on any $S-D$ transition can be realized by resonantly driving the corresponding transition line using a narrow-linewidth laser at 729 nm, where θ is the rotation angle, ϕ is the laser phase, and σ_x^m, σ_y^m are Pauli matrices. Using the digital

quantum simulation method, the state preparation and arbitrary unitary operation can be decomposed into appropriate sequences of $S-D$ equatorial rotations. The states in the S manifold can be identified via state-dependent fluorescence observed using a photomultiplier tube (PMT) [37], while coupling the $S_{1/2}$ state to the short-lived state $P_{1/2}$ (with a lifetime 7.1 ns) by a laser field at 397 nm. With the help of appropriate $S-D$ rotations, this photon fluorescence detection method enables us to access populations p_1 and p_2, and post-select the experimental sequences, where the $\mathcal{PT}$-symmetric dynamics is successfully performed. A more detailed description of the experimental setup and model derivation can be found in Supplementary Material.

Using the dilation method [38], we embed the $\mathcal{PT}$-symmetric dynamics into a directed sum of two 2-dimensional Hilbert spaces $\mathcal{H}_S$ and $\mathcal{H}_A$, where $\mathcal{H}_S$ and $\mathcal{H}_A$ are expanded by $\{|1\rangle, |2\rangle\}$ and $\{|3\rangle, |4\rangle\}$, respectively (FIG. 2c). We first prepare the total system into the initial state $|\Psi(\tau=0)\rangle = N(|\psi\rangle_0 \oplus \eta\,|\psi\rangle_0)$, where $\eta = \frac{1}{\Omega}[J, -\mathrm{i}\Gamma; \mathrm{i}\Gamma, J]$ is the metric operator for $\hat{H}_{\mathrm{PT}}$ satisfying $\eta = \eta^\dagger$ and $\eta\hat{H}_{\mathrm{PT}} = \hat{H}_{\mathrm{PT}}^\dagger\eta$, and N is the normalization factor. The unitary operation

$$U = \begin{pmatrix} F & G \\ -G & F \end{pmatrix} \tag{4}$$

is then enforced on the composite space $\mathcal{H}_S \bigoplus \mathcal{H}_A$, where the block matrices are $F = \cos(\tau)I_2^m - \mathrm{i}\frac{\Omega}{J}\sin(\tau)\sigma_x^m$ and $G = \frac{\Gamma}{J}\sin(\tau)\sigma_z^m$; I_2^m is the 2-dimensional identity matrix, and σ_x^m and σ_z^m are usual Pauli matrices. After the desired evolution, a post-selection procedure is performed to discard the cases where the space $\mathcal{H}_A$ is occupied. Finally, we achieve the $\mathcal{PT}$-symmetric dynamics $\hat{U}_{\mathrm{PT}}|\psi\rangle_0$ in $\mathcal{H}_S$. The probability of the successful post-selection can be obtained as

$$p_{\mathrm{suc}} = \mathrm{Tr}[\mathrm{N}^2\hat{\mathrm{U}}_{\mathrm{PT}}|\psi\rangle_{00}\langle\psi|\hat{\mathrm{U}}_{\mathrm{PT}}^\dagger]. \tag{5}$$

In FIG. 2d, we experimentally verify the nonlinear dynamics described by Eq. (3). The post-selection probability p_{suc}, and the normalized population of the state $|1\rangle$, denoted as p_1^n, are plotted versus the scaled time $\tau = \Omega t$, with $\Gamma/J = 0$, 0.5 and 0.95. The quantum power oscillation phenomenon can be observed in the periodic oscillatory behavior of the probabilities of the successful post-selection. And it is shown from the measured results of p_1^n that, as the ratio Γ/J becomes larger, the uneven flip speed caused by the nonlinear term becomes more pronounced.

To realize the accelerated dynamics in the one-way flip via the nonlinear term of Eq. (3), similar to the non-Hermitian coin in FIG. 1b, we need to drive the $\mathcal{PT}$-symmetric qubit from the appropriate superposition state. Based on a tomography technique, we experimentally study the flip dynamics of the qubit from $|-\rangle_y = \frac{1}{\sqrt{2}}(|1\rangle - \mathrm{i}\,|2\rangle)$ to $|+\rangle_y = \frac{1}{\sqrt{2}}(|1\rangle + \mathrm{i}\,|2\rangle)$ with $\Gamma/J = 0$, 0.5 and 0.95 [FIG. 3(a-c)]. The time intervals

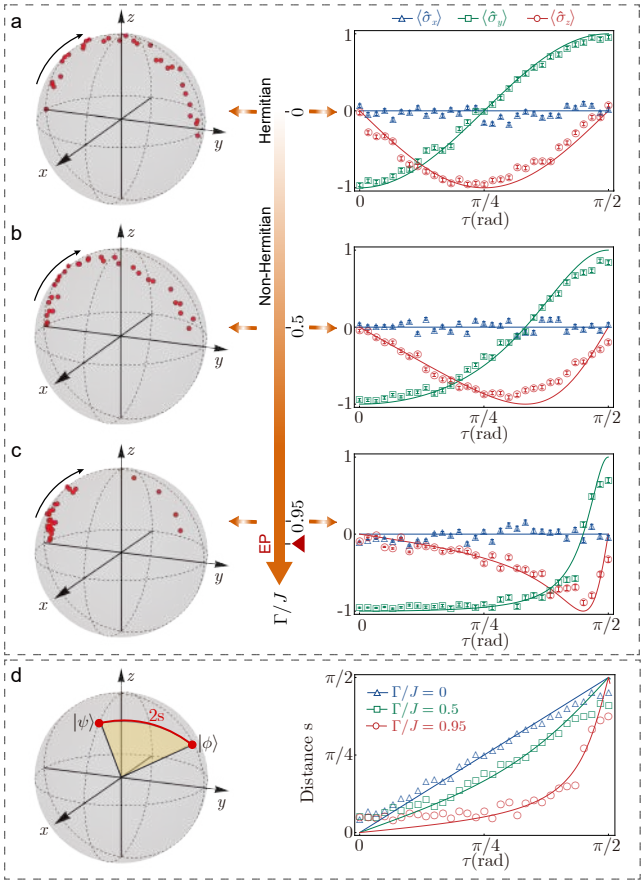

FIG. 3. **Accelerated dynamics manifested by the $\mathcal{PT}$-symmetric qubit. a-c**, The Bloch vector (left) and its components (right) versus time τ for $\Gamma/J = 0$ (**a**), $\Gamma/J = 0.5$ (**b**) and $\Gamma/J = 0.95$ (**c**), when driving the qubit from $|-\rangle_y$ to $|+\rangle_y$. Both the dense-to-sparse behavior of the Bloch vector data and the asymmetric features in the $\langle\hat{\sigma}_y\rangle$ and $\langle\hat{\sigma}_z\rangle$ components indicate the accelerated dynamics when $\Gamma/J > 0$. **d**, The distance s from the initial state, defined as half the geodesic distance on the Bloch sphere, is experimentally measured versus τ for various Γ/J, which shows a nonuniform flip speed in the non-Hermitian realm. When $\Gamma/J \to 1$, i. e. close to the exceptional point (EP), the flip dynamics similar to the non-Hermitian case in FIG. 1b occurs.

between adjacent data points of the Bloch vector [left of FIG. 3(a-c)] and its components [right of FIG. 3(a-c)] are equal. The initial state and Hamiltonian confine the evolution to the $y-z$ plane of the Bloch sphere. With the increase of Γ/J, the accelerated dynamics becomes visible, which can be reflected by the dense-to-sparse behavior of the Bloch vector data points. The Bloch vector components versus time, plotted for different values of Γ/J, show a good agreement with our theoretical predictions, and the asymmetric features in the curves of y and z components when $\Gamma/J > 0$ also demonstrate the acceleration properties. By introducing the Fubini-Study metric $s = \arccos|\langle\psi|\phi\rangle|$, as the distance between quantum states $|\psi\rangle$ and $|\phi\rangle$ [39], we can indirectly study the charac-

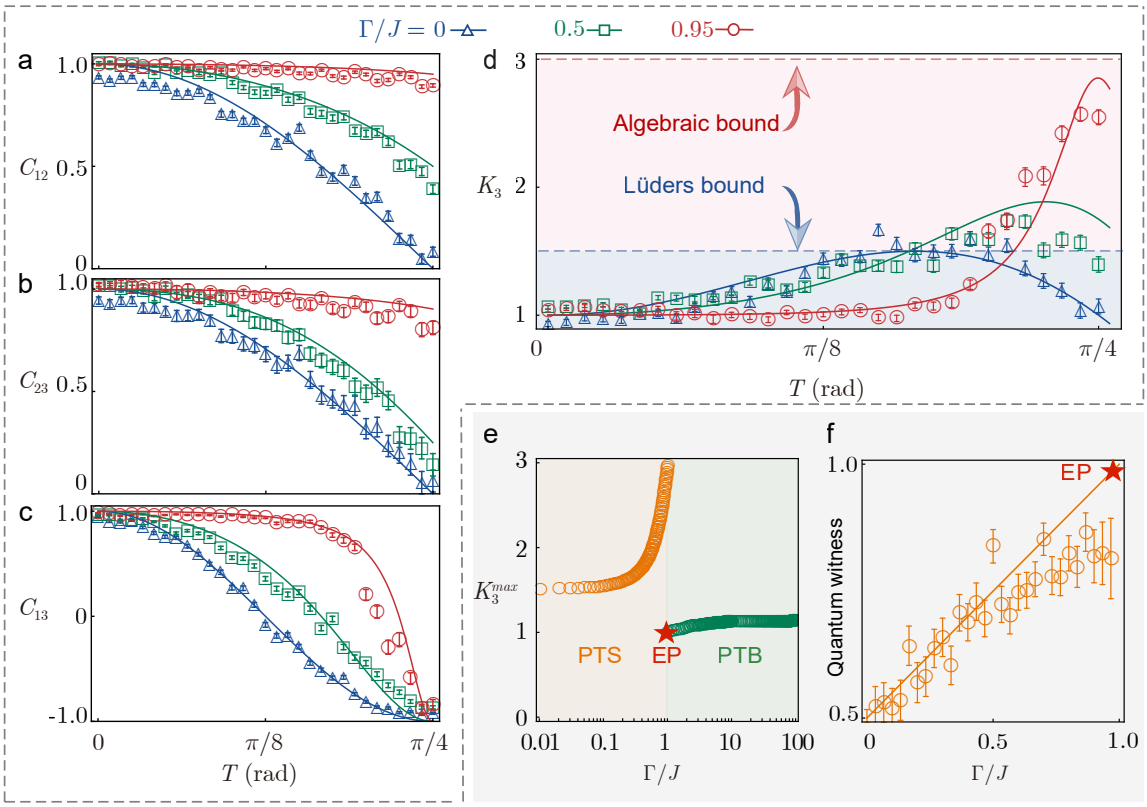

FIG. 4. **Leggett-Garg parameter K_3 and quantum witness for the $\mathcal{PT}$-symmetric qubit. a-d**, The measured correlation functions C_{12} (**a**), C_{23} (**b**), C_{13} (**c**), and the Leggett-Garg parameter K_3 (**d**) are plotted versus the measurement time interval T for $\Gamma/J = 0$, 0.5 and 0.95. It shows that, K_3 asymptotically approaches its algebraic bound of 3 when close to the EP. **e**, The maximal temporal quantum correlations $K_3^{\max}$, obtained by theoretical optimization, in both $\mathcal{PT}$-symmetric unbroken (PTS) and broken (PTB) regions. **f**, The experimentally measured quantum witness for various values of Γ/J, which also asymptotically approaches its algebraic bound of 1 when close to the EP.

teristics of the evolution speed $\nu = \frac{\mathrm{d}s}{\mathrm{d}\tau}$ in the flip process (FIG. 3d). For the qubit, the distance s is geometrically half the geodesic distance on the Bloch sphere between $|\psi\rangle$ and $|\phi\rangle$. It is shown that, when $\Gamma/J = 0$, s increases linearly and the Hermitian qubit evolves with a uniform speed. In the non-Hermitian realm with $\Gamma/J > 0$, the slopes in the plots of s show increasing trends of the evolution speed with increasing τ. An interesting result is that, when $\Gamma/J \to 1$, i. e. close to the EP, the flip process similar to the non-Hermitian coin in FIG. 1b occurs.

Using the above accelerated evolution characteristics manifested in such a $\mathcal{PT}$-symmetric qubit, we can achieve the temporal quantum correlation beyond the Lüders bound. In our experiment, the two-time correlation functions are indirectly computed via the experimentally measured conditional probability $p_\tau(Q'|Q)$, for observing the measurement outcome Q' at the scaled time τ given that we deterministically initialize the qubit in the eigenstate $|Q\rangle$. For testing the temporal Bell inequality, we prepare the qubit in $|-\rangle_y$, choose the three scaled time instants as $\tau_1 = 0$, $\tau_2 = T$, and $\tau_3 = 2T$, and set the Pauli operator $\hat{\sigma}_y$ as the physical observable, then the two-time correlation functions can be given by

$$\begin{cases} C_{12} &= -p_{\mathrm{T}}(+|-) + p_{\mathrm{T}}(-|-), \\ C_{13} &= -p_{2\mathrm{T}}(+|-) + p_{2\mathrm{T}}(-|-), \\ C_{23} &= p_{\mathrm{T}}(+|-)p_{\mathrm{T}}(+|+) - p_{\mathrm{T}}(+|-)p_{\mathrm{T}}(-|+) \\ & \quad -p_{\mathrm{T}}(-|-)p_{\mathrm{T}}(+|-) + p_{\mathrm{T}}(-|-)p_{\mathrm{T}}(-|-). \end{cases} \tag{6}$$

The experimental results for C_{12}, C_{13} and C_{23} as functions of the scaled time interval $T \in [0, \frac{\pi}{4}]$ for $\Gamma/J = 0$, 0.5 and 0.95 are given in FIG. 4(a-c). Because the non-Hermiticity can cause the slow flip speed of the qubit at the beginning, a larger $\frac{\Gamma}{J}$ can make the qubit states at times τ_1 and τ_2 more positively correlated, and eventually leads to a larger correlation function C_{12} (FIG. 4a). The measurement performed at time τ_2 collapses the superposition state into a mixture of $|+\rangle_y$ and $|-\rangle_y$, making the subsequent evolution as slow as the initial time, so the plot of C_{23} has a similar behavior as C_{12} (FIG. 4b). However, without performing such a measurement, the qubit always finishes a complete flip in the time period $[0, \frac{\pi}{2}]$ independent of $\frac{\Gamma}{J}$. Therefore, the plots C_{13} converge to -1 when $T = \frac{\pi}{4}$ (FIG. 4c). Based on these data of the two-time correlation functions, the Leggett-Garg parameter

K_3 is plotted in FIG. 4d. It is seen that, in the Hermitian regime ($\frac{\Gamma}{J}=0$), K_3 is bounded by the Lüders bound of 1.5. However, in the non-Hermitian regime ($\frac{\Gamma}{J}>0$), K_3 obviously breaks this upper bound. For $\frac{\Gamma}{J}=0.95$, we experimentally observe the Leggett-Garg parameter as large as $K_3=2.57\pm0.08$.

Note that the dilation method [38] used here cannot experimentally reach the $\mathcal{PT}$-symmetric broken region (PTB). However, in FIG. 4e, we give the values of the maximal temporal quantum correlation $K_3^{\max}$ in both the PTS and PTB regions, obtained by theoretically maximizing K_3 when varying the measurement interval T in our measurement model (see Supplementary Material for details). It is shown that, $K_3^{\max}$ suddenly drops from the algebraic bound of 3 to about 1 at the EP, which is due to the abrupt transition from the oscillatory dynamics to the decay dynamics when crossing the PTS-PTB region boundary.

The quantum witness W [40], which is another indicator of temporal quantum correlations, is also tested in our experiment. It is defined as

$$W=|p'(Q)-p(Q)|, \tag{7}$$

where $p'(Q)$ and $p(Q)$ are the probabilities for observing the measurement outcome Q after a period of system's evolution in the presence and absence of an earlier measurement performed on the initial state, respectively. Here, $p'(Q)$ can be computed as $p'(Q)=\sum_{Q_0=\pm1}p(Q|Q_0)p(Q_0)$, where $p(Q_0)$ is the probability of obtaining an outcome Q_0 for the initial measurement, and $p(Q|Q_0)$ is the probability of finding an outcome Q for the later measurement conditional on the initial outcome Q_0. For a macrorealistic system, the initial measurement should not disturb the outcomes of the later measurement, which leads to $W\equiv0$. For a Hermitian quantum system, the quantum witness is bounded by

$$0\le W\le 1-\frac{1}{D}, \tag{8}$$

where D is the dimension of the Hilbert space of the system. Therefore, W can be used as an effective dimensional witness for the quantum systems. Specially, $W\le\frac{1}{2}$ holds for a Hermitian qubit. In the experiment, we initialize the qubit in $|\psi\rangle_0=(-\sqrt{J-\Gamma}\,|+\rangle_y+\sqrt{J+\Gamma}\,|-\rangle_y)/\sqrt{2J}$, choose the observable $\hat{\sigma}_y$, set the scaled evolution time prior to the later measurement as $\frac{\pi}{4}$, and compare the probabilities of obtaining the outcome $Q=+1$ in the two measurement scenarios. Then, the quantum witness W for different values of $\frac{\Gamma}{J}$ is plotted in FIG. 4f. It is shown that, in the Hermitian realm ($\frac{\Gamma}{J}=0$), we experimentally obtain the upper bound of the quantum witness determined by Eq. (8). When $\frac{\Gamma}{J}>0$, the introduced non-Hermiticity can help to break the upper bound for the Hermitian case. More interestingly, when we get close to the EP ($\frac{\Gamma}{J}\to1$), the quantum witness asymptotically approaches its algebraic maximum of 1 which is otherwise observed for a Hermitian system with infinite dimensional Hilbert space.

In conclusion, this work constitutes the first experimental characterization of the temporal correlation features in non-Hermitian quantum systems. For both the Leggett-Garg parameter and the quantum witness, we have observed a clear breakthrough of the upper bounds for the Hermitian case, and experimentally approached their algebraic bounds near the exceptional point of a $\mathcal{PT}$-symmetric qubit, which have never been reached previously in the standard measurement scenario. We elucidate a direct connection between the non-Hermiticity-induced nonlinear dynamics and the enhanced temporal quantum correlation. Due to the fundamental importance of correlation properties in quantum mechanics, our study motivates a new perspective to re-examine the core issues and intriguing phenomena related to non-Hermitian quantum systems. Furthermore, our successful demonstration of nonlinear dynamics in the simple atomic system may serve as a tool to explore many fundamental questions in quantum mechanics, such as quantum chaos [41], nonequilibrium dynamics in few-body quantum systems [42], and quantum speed limits [39].

Acknowledgements

This work was supported by the National Natural Science Foundation of China (Grant Nos. 12174448, 12174447, 12074433, 12004430, 11904402, 12204543, and 11935006), the Innovation Program for Quantum Science and Technology (2021ZD0301601) and the Science and Technology Innovation Program of Hunan Province (2022RC1194, 2023JJ10052, and 2020RC4047).

Competing financial interests

The authors declare no competing financial interests.

[1] J. S. Bell, On the Einstein Podolsky Rosen paradox, Physics **1**, 195 (1964).
[2] A. J. Leggett and A. Garg, Quantum mechanics versus macroscopic realism: is the flux there when nobody looks, Phys. Rev. Lett. **54**, 857 (1985).
[3] Y. Ashida, Z. Gong, and M. Ueda, Non-Hermitian physics, Adv. Phys. **69**, 249 (2020).
[4] R. El-Ganainy, K. G. Makris, M. Khajavikhan, Z. H. Musslimani, and D. N. Christodoulides, Non-Hermitian physics and PT symmetry, Nat. Phys. **14**, 11 (2018).
[5] K. Modi, A. Brodutch, H. Cable, T. Paterek, and V. Vedral, The classical-quantum boundary for correlations: discord and related measures, Rev. Mod. Phys. **84**, 1655 (2012).
[6] C. Emary, N. Lambert, and F. Nori, Leggett–Garg inequalities, Rep. Prog. Phys. **77**, 016001 (2013).

[7] G. S. Engel, T. R. Calhoun, E. L. Read, T. K. Ahn, T. Mancal, Y. C. Cheng, R. E. Blankenship, and G. R. Fleming, Evidence for wavelike energy transfer through quantum coherence in photosynthetic systems, Nature **446**, 782 (2007).

[8] G. Panitchayangkoon, D. Hayes, K. A. Fransted, J. R. Caram, E. Harel, J. Wen, R. E. Blankenship, and G. S. Engel, Long-lived quantum coherence in photosynthetic complexes at physiological temperature, Proc. Natl. Acad. Sci. USA **107**, 12766 (2010).

[9] M. M. Wilde, J. M. Mccracken, and A. Mizel, Could light harvesting complexes exhibit non-classical effects at room temperature, Proc. R. Soc. A **466**, 1347 (2010).

[10] N. Lambert, C. Emary, Y. Chen, and F. Nori, Distinguishing quantum and classical transport through nanostructures, Phys. Rev. Lett. **105**, 176801 (2010).

[11] C. M. Li, N. Lambert, Y. N. Chen, G. Y. Chen, and F. Nori, Witnessing quantum coherence: from solid-state to biological systems, Sci. Rep. **2**, 885 (2012).

[12] A. M. Souza, J. Li, D. O. Soares-Pinto, R. S. Sarthour, I. S. Oliveira, S. F. Huelga, M. Paternostro, and F. L. Semião, Experimental demonstration of non-Markovian dynamics via a temporal Bell-like inequality, arXiv:1308.5761 (2013).

[13] M. Howard, J. Wallman, V. Veitch, and J. Emerson, Contextuality supplies the 'magic' for quantum computation, Nature **510**, 351–355 (2014).

[14] F. Morikoshi, Information-theoretic temporal Bell inequality and quantum computation, Phys. Rev. A **73**, 485 (2006).

[15] A. Palacios-Laloy, F. Mallet, F. Nguyen, P. Bertet, D. Vion, D. Esteve, and A. N. Korotkov, Experimental violation of a Bell's inequality in time with weak measurement, Nat. Phys. **6**, 442 (2010).

[16] J. P. Groen, D. Ristè, L. Tornberg, J. Cramer, P. C. de Groot, T. Picot, G. Johansson, and L. Dicarlo, Partial-measurement backaction and nonclassical weak values in a superconducting circuit, Phys. Rev. Lett. **111**, 090506 (2013).

[17] G. Waldherr, P. Neumann, S. F. Huelga, F. Jelezko, and J. Wrachtrup, Violation of a temporal Bell inequality for single spins in a diamond defect center, Phys. Rev. Lett. **107**, 090401 (2011).

[18] R. E. George, L. M. Robledo, O. J. E. Maroney, M. S. Blok, H. Bernien, M. L. Markham, D. J. Twitchen, J. J. L. Morton, G. A. D. Briggs, and R. Hanson, Opening up three quantum boxes causes classically undetectable wavefunction collapse, Proc. Natl. Acad. Sci. USA **110**, 3777 (2013).

[19] V. Athalye, S. S. Roy, and T. S. Mahesh, Investigation of the Leggett-Garg inequality for precessing nuclear spins, Phys. Rev. Lett. **107**, 130402 (2011).

[20] M. E. Goggin, M. P. Almeida, M. Barbieri, B. P. Lanyon, J. L. O'Brien, A. G. White, and G. J. Pryde, Violation of the Leggett-Garg inequality with weak measurements of photons, Proc. Natl. Acad. Sci. USA **108**, 1256 (2011).

[21] J. Dressel, C. J. Broadbent, J. C. Howell, and A. N. Jordan, Experimental violation of two-party Leggett-Garg inequalities with semi-weak measurements, Phys. Rev. Lett. **106**, 040402 (2011).

[22] G. C. Knee, S. Simmons, E. M. Gauger, J. J. Morton, H. Riemann, N. V. Abrosimov, P. Becker, H. J. Pohl, K. M. Itoh, M. L. Thewalt, G. A. D. Briggs, and S. C. Benjamin, Violation of a Leggett-Garg inequality with ideal non-invasive measurements, Nat. Commun. **3**, 606 (2012).

[23] Z. Q. Zhou, S. F. Huelga, C. F. Li, and G. C. Guo, Experimental detection of quantum coherent evolution through the violation of Leggett-Garg-type inequalities, Phys. Rev. Lett. **115**, 113002 (2015).

[24] J. A. Formaggio, D. I. Kaiser, M. M. Murskyj, and T. E. Weiss, Violation of the Leggett-Garg inequality in neutrino oscillations, Phys. Rev. Lett. **117**, 050402 (2016).

[25] G. C. Knee, K. Kakuyanagi, M. C. Yeh, Y. Matsuzaki, H. Toida, H. Yamaguchi, S. Saito, A. J. Leggett, and W. J. Munro, A strict experimental test of macroscopic realism in a superconducting flux qubit, Nat. Commun. **7**, 13253 (2016).

[26] H. Y. Ku, N. Lambert, F. J. Chan, C. Emary, and F. Nori, Experimental test of non-macrorealistic cat states in the cloud, NPJ Quantum Inf. **6**, 98 (2020).

[27] K. Wang, M. Xu, L. Xiao, and P. Xue, Experimental violations of Leggett-Garg inequalities up to the algebraic maximum for a photonic qubit, Phys. Rev. A **102**, 022214 (2020).

[28] C. Budroni and C. Emary, Temporal quantum correlations and Leggett-Garg inequalities in multilevel systems, Phys. Rev. Lett. **113**, 050401 (2014).

[29] H. Katiyar, A. Brodutc, D. Lu, and R. Laflamme, Experimental violation of the Leggett–Garg inequality in a three-level system, New J. Phys. **19**, 023033 (2017).

[30] K. Wang, C. Emary, X. Zhan, Z. Bian, J. Li, and P. Xue, Enhanced violations of Leggett-Garg inequalities in an experimental three-level system, Opt. Express **25**, 31462 (2017).

[31] M. Tusun, W. Cheng, Z. Chai, Y. Wu, Y. Wang, X. Rong, and J. Du, Experimental violation of the Leggett-Garg inequality with a single-spin system, Phys. Rev. A **105**, 042613 (2022).

[32] T. Zhan, C. Wu, M. Zhang, Q. Qin, X. Yang, H. Hu, W. Su, J. Zhang, T. Chen, Y. Xie, W. Wu, and P. Chen, Experimental violation of the Leggett-Garg inequality in a three-level trapped-ion system, Phys. Rev. A **107**, 012424 (2023).

[33] H. S. Karthik, H. Akshata Shenoy, and A. R. Usha Devi, Leggett-Garg inequalities and temporal correlations for a qubit under PT-symmetric dynamics, Phys. Rev. A **103**, 032420 (2021).

[34] A. V. Varma, I. Mohanty, and S. Das, Temporal correlation beyond quantum bounds in non-Hermitian PT-symmetric dynamics of a two level system, J. Phys. A **54**, 115301 (2021).

[35] C. E. Rüter, K. G. Makris, R. El-Ganainy, D. N. Christodoulides, M. Segev, and D. Kip, Observation of parity–time symmetry in optics, Nat. Phys. **6**, 192 (2010).

[36] D. C. Brody and E. M. Graefe, Mixed-state evolution in the presence of gain and loss, Phys. Rev. Lett. **109**, 230405 (2012).

[37] A. H. Myerson, D. J. Szwer, S. C. Webster, D. T. C. Allcock, M. J. Curtis, G. Imreh, J. A. Sherman, D. N. Stacey, A. M. Steane, and D. M. Lucas, High-fidelity readout of trapped-ion qubits, Phys. Rev. Lett. **100**, 200502 (2008).

[38] U. Günther and B. F. Samsonov, Naimark-dilated PT-symmetric brachistochrone, Phys. Rev. Lett. **101**, 230404 (2008).

[39] J. Anandan and Y. Aharonov, Geometry of quantum evo-

lution, Phys. Rev. Lett. **65**, 1697 (1990).
[40] G. Schild and C. Emary, Maximum violations of the quantum-witness equality, Phys. Rev. A **92**, 032101 (2015).
[41] L. D'Alessio, Y. Kafri, A. Polkovnikov, and M. Rigol, From quantum chaos and eigenstate thermalization to statistical mechanics and thermodynamics, Adv. Phys. **65**, 239 (2016).
[42] A. Polkovnikov, K. Sengupta, A. Silva, and M. Vengalattore, Colloquium: nonequilibrium dynamics of closed interacting quantum systems, Rev. Mod. Phys. **83**, 863 (2011)

SUPPLEMENT

In the Supplementary Material, we describe our experimental setup and used techniques in more detail, and also give the theoretical analysis for quantum temporal correlations in our parity-time ($\mathcal{PT}$)-symmetric model.

A. Experimental setup

All the relevant energy levels involved in this experiment are shown in Fig. S.1(a). Four of the Zeeman sublevels (labeled $|1\rangle$, $|2\rangle$, $|3\rangle$ and $|4\rangle$) in $S_{1/2}$ and $D_{5/2}$ states of a single trapped $^{40}Ca^{+}$ ion are used to simulate the active parity-time ($\mathcal{PT}$)-symmetric dynamics, and the transitions between these sublevels have least sensitivity to the fluctuations of the magnetic field, which makes these energy levels to have a coherence time of several milliseconds. The coherent couplings between these states are realized by applying a narrow-linewidth 729 nm laser beam with its wavevector along the axial direction of the linear Paul trap. Although only carrier transitions are used in this experiment, we still use the Doppler cooling and electromagnetically induced transparency (EIT) cooling methods [1] to prepare the motional degree of the freedom to the ground state, which guarantees high-fidelity operations of the single $\mathcal{PT}$-symmetric qubit. Laser frequencies for different transitions are reached by tuning the driving frequency of a single-pass acousto-optical modulator (AOM), which is labeled AOM 1 in Fig. S.1(b). The 397 nm laser is used for Doppler cooling, EIT cooling, and fluorescence detection. The 866 nm and 854 nm lasers are used to pumping the ion out from D states. To reduce the influence of the ac Stark effect, the Rabi frequency of each transition is set to about $2\pi\times$ 10 kHz, which induces an estimated ac Stark shift of less than 50 Hz in the experiment. In this case, we can ignore the influence from the ac Stark shift.

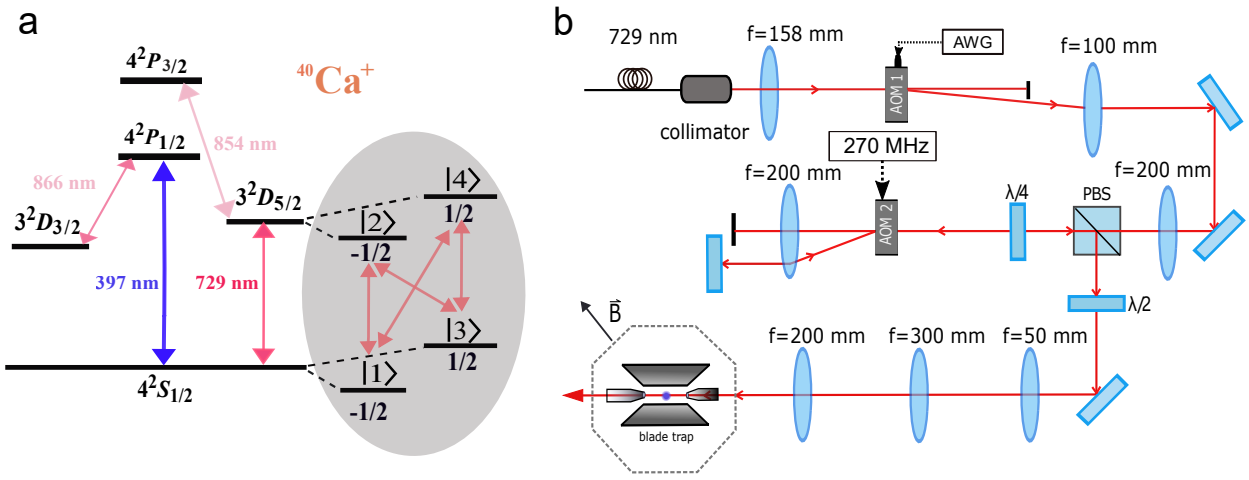

FIG. S.1. (a) Relevant energy levels used in our experiment. The coherent coupling between the S and D states is realized by using a narrow-linewidth 729 nm laser beam, while the 397 nm laser is used for cooling and detection processes. (b) Optical setup for the 729 nm laser, which is modulated by two acousto-optical modulators (AOMs) with a single pass and a double pass configurations, respectively. The single-pass AOM (labeled AOM1) is driven by an arbitrary wave generator (AWG) to control the intensity, frequency, and phase of the laser pulses, while the double-pass AOM (labeled AOM2) is used to shift the laser frequency close to the resonance of $S-D$ transition. The 729-nm laser beam finally enters the blade linear Paul trap by passing through two hollow end-cap electrodes with an angle of 0° to the axial direction.

B. Experimental techniques

1. *Initial state preparation and evolution operator decomposition*

The resonant coupling between each pair of the four Zeeman sublevels, as shown in Fig. S.1(a), can be described by the equatorial rotations

$$R_{ij}(\theta,\phi)=\exp\Big\{-i\theta[\cos(\phi)\sigma_x^m+\sin(\phi)\sigma_y^m]/2\Big\}, \tag{S.1}$$

where i and j indicate the addressed transition, σ_x^m, σ_y^m are the Pauli x, y matrices, and θ is the rotation angle. The rotation phase ϕ is the laser phase when $|i\rangle$ is in the S manifold, but we need to add a negative sign when $|j\rangle$ is S state.

Taking advantage of above elementary operations and the decomposition method described in Ref. [2], the initial state preparation and unitary evolutionary operation in our experiment can be realized via applying an appropriate series of $S-D$ equatorial rotations. All the state preparation starts from the same state $|1\rangle = (1,0,0,0)^T$. Now, we introduce the metric operator $\eta = \frac{1}{\Omega}[J, -i\Gamma; i\Gamma, J]$ for $\hat{H}_{\mathrm{PT}}$ [3], where J and Γ are the coupling and loss (gain) rates of our $\mathcal{PT}$-symmetric system, $\Omega = \sqrt{J^2-\Gamma^2}$ denotes the effective oscillation frequency. To simplify the mathematical expressions, we define the parameter $\sin(\alpha) = \Gamma/J$. The initial states used in our experiment and their preparation sequences are summarized in the following Table S.1, where η means the metric operator we have introduced (a more detailed construction process of η is elaborated in Sec. E 2).

TABLE S.1. Target initial states and the corresponding preparation sequences.

Unnormalized target initial state	Preparation sequence	State in figures
$\begin{pmatrix}0\\1\end{pmatrix} \oplus \eta \begin{pmatrix}0\\1\end{pmatrix}$	$R_{34}(\theta_2,\pi)\cdot R_{23}(\theta_1,0)\cdot R_{12}(\pi,0)$ $\theta_2 = 2\arccos\left(\frac{\tan(\alpha)}{\sqrt{\sec(\alpha)^2+\tan(\alpha)^2}}\right)$ $\theta_1 = 2\arccos\left(\frac{\cos(\alpha)}{\sqrt{2}}\right)$	Fig. 2(e)
$\begin{pmatrix}1\\-i\end{pmatrix} \oplus \eta \begin{pmatrix}1\\-i\end{pmatrix}$	$R_{34}(\theta_2,\pi)\cdot R_{12}(\theta_1,0)\cdot R_{14}(\theta_0,0)$ $\theta_2 = \pi/2$ $\theta_1 = \pi/2$ $\theta_0 = 2\,\mathrm{arcsec}\left(\sqrt{1+(\sec(\alpha)-\tan(\alpha))^2}\right)$	Fig. 3 Fig. 4(a-d)
$\begin{pmatrix}1\\i\end{pmatrix} \oplus \eta \begin{pmatrix}1\\i\end{pmatrix}$	$R_{34}(\theta_2,0)\cdot R_{12}(\theta_1,\pi)\cdot R_{14}(\theta_0,\pi)$ $\theta_2 = \pi/2$ $\theta_1 = \pi/2$ $\theta_0 = 2\arctan(\tan(\alpha)+\sec(\alpha))$	Fig. 4(a-d)
$\begin{pmatrix}\cos(\gamma)-\sin(\gamma)\\-i\cos(\gamma)-i\sin(\gamma)\end{pmatrix} \oplus \eta \begin{pmatrix}\cos(\gamma)-\sin(\gamma)\\-i\cos(\gamma)-i\sin(\gamma)\end{pmatrix}$	$R_{34}(\theta_2,\pi)\cdot R_{12}(\theta_1,0)\cdot R_{14}(\theta_0,0)$ $\theta_2 = 2\arcsin\left(\frac{\cos(\gamma)-\sin(\gamma)-\sin(\alpha)(\cos(\gamma)+\sin(\gamma))}{\sqrt{3-\cos(2\alpha)-4\cos(2\gamma)\sin(\alpha)}}\right)$ $\theta_1 = 2\arccos\left(\frac{\cos(\gamma)-\sin(\gamma)}{\sqrt{2}}\right)$ $\theta_0 = 2\arccos\left(\frac{\cos(\alpha)}{\sqrt{2-2\cos(2\gamma)\sin(\alpha)}}\right)$ $\gamma = \arcsin\left(\sqrt{\frac{J-\Gamma}{2J}}\right)$	Fig. 4(f)

The dynamic evolution after the state preparation is described by a unitary operator $U(\alpha,\tau)$, which can be decomposed into four equatorial rotations in the experiment. Theoretical construction process of $U(\alpha,\tau)$ is introduced in Sec. E 1. Its concrete form and experimental execution sequence can be written as

$$
\begin{aligned}
U(\alpha,\tau) &= \begin{pmatrix} \cos(\tau) & -i\cos(\alpha)\sin(\tau) & \sin(\tau)\sin(\alpha) & 0 \\ -i\cos(\alpha)\sin(\tau) & \cos(\tau) & 0 & -\sin(\tau)\sin(\alpha) \\ -\sin(\tau)\sin(\alpha) & 0 & \cos(\tau) & -i\cos(\alpha)\sin(\tau) \\ 0 & \sin(\tau)\sin(\alpha) & -i\cos(\alpha)\sin(\tau) & \cos(\tau) \end{pmatrix} \\
&= R_{23}(2\alpha,0)R_{12}(2\tau,0)R_{34}(2\tau,0)R_{23}(2\alpha,\pi),
\end{aligned}
\tag{S.2}
$$

where $\tau = \Omega t$ is the scaled time.

2. State detection and population normalization

In the detection process, we only need to extract the populations of the states $|1\rangle$ and $|2\rangle$, which are labeled as p_1 and p_2. However, populations may distributed in four states in the evolution. Two equatorial rotations and two fluorescence detection processes are employed to distinguish the states $|1\rangle$ and $|2\rangle$ from the subspace consisting of $|3\rangle$ and $|4\rangle$. The first step includes a π-pulse rotation $R_{14}(\pi, 0)$ and a following fluorescence detection, then another $R_{14}(\pi, 0)$ is used to swap the states back and the fluorescence detection is applied again in the second step. For the results obtained in above steps, the bright state in the first step denotes the population out of the subspace $\mathcal{H}_S = \{|1\rangle, |2\rangle\}$, the dark state in the first step combined with the bright state in the second step gives the population p_1, and the dark states in both steps give the result for p_2.

In the experiment, the total population $p = p_1 + p_2$ for $\mathcal{H}_S$ exhibits periodic oscillatory behavior, which is a quantum version of the power oscillation phenomenon in classical $\mathcal{PT}$-symmetric system. By introducing the normalized populations $p_1^n = \frac{p_1}{p_1+p_2}$ and $p_2^n = \frac{p_2}{p_1+p_2}$, we can experimentally obtain the normalized dynamics of a $\mathcal{PT}$-symmetric qubit described by Eq. (3) of the main text .

3. Quantum state tomography

To manifest accelerated dynamics shown in Fig. 3, a quantum state tomography technique is used to study the dynamic evolution of the $\mathcal{PT}$-symmetric qubit, which can obtain the full information of the Bloch vector at each moment. The z component of the Bloch vector, denoted as $\langle\hat{\sigma}_z\rangle$, can be directly extracted by experimentally measuring the difference of the normalized populations p_1^n and p_2^n. The x (y) component, denoted as $\langle\hat{\sigma}_x\rangle$ ($\langle\hat{\sigma}_y\rangle$), can be obtained by the combination of an extra equatorial rotation $R_{12}(3\pi/2, \pi/2)$ [$R_{12}(\pi/2, 0)$] and the following detection procedure of $\langle\hat{\sigma}_z\rangle$. Finally, the maximum likelihood estimation method is utilized to reduce the statistical and systematic errors.

C. Measurement of the correlation functions

Our test of the temporal Bell inequality chooses three scaled time instants, labeled as $\tau_1 = 0$, $\tau_2 = T$ and $\tau_3 = 2T$. The two-time correlation functions, C_{12}, C_{13}, and C_{23}, can be indirectly measured via the conditional probability $p_\tau(Q^{'}|Q)$, for observing the measurement outcome $Q^{'}$ at the scaled time τ given that we deterministically initialize the qubit in the eigenstate $|Q\rangle$. In the experiment, $p_{_T}(+|-)$ [$p_{_{2T}}(+|-)$] is measured by preparing the initial state in $|-\rangle_y$, then applying the evolution operation $U(\alpha, T)$ [$U(\alpha, 2T)$], and finally measuring the probability distribution of the physical observable $\hat{\sigma}_y$. The conditional probabilities $p_{_T}(-|-)$ and $p_{_{2T}}(-|-)$ can be obtained by the normalization relations $p_{_T}(+|-)+p_{_T}(-|-) = 1$ and $p_{_{2T}}(+|-)+p_{_{2T}}(-|-) = 1$, respectively. Similar procedure is performed to obtain the conditional probabilities $p_{_T}(+|+)$ and $p_{_T}(-|+)$. Based on the above experimental data, C_{12}, C_{13}, and C_{23} can be obtained using Eq. (6) in the main text. In Fig. S.2, we show our experimental results for the obtained conditional probabilities and the correlation functions, and the error bars are calculated by the binomial distributions of p_1^n and p_2^n.

D. Measurement of the quantum witness W

To measure the quantum witness

$$W = |p'(Q) - p(Q)| \tag{S.3}$$

experimentally, $p'(Q)$ and $p(Q)$ should be addressed separately. The probability $p(Q)$, which indicates the probability for observing the outcome Q without earlier measurement, can be obtained by preparing the initial state

$$|\psi\rangle_0 = -\frac{\sqrt{J-\Gamma}}{\sqrt{2J}}|+\rangle_y + \frac{\sqrt{J+\Gamma}}{\sqrt{2J}}|-\rangle_y, \tag{S.4}$$

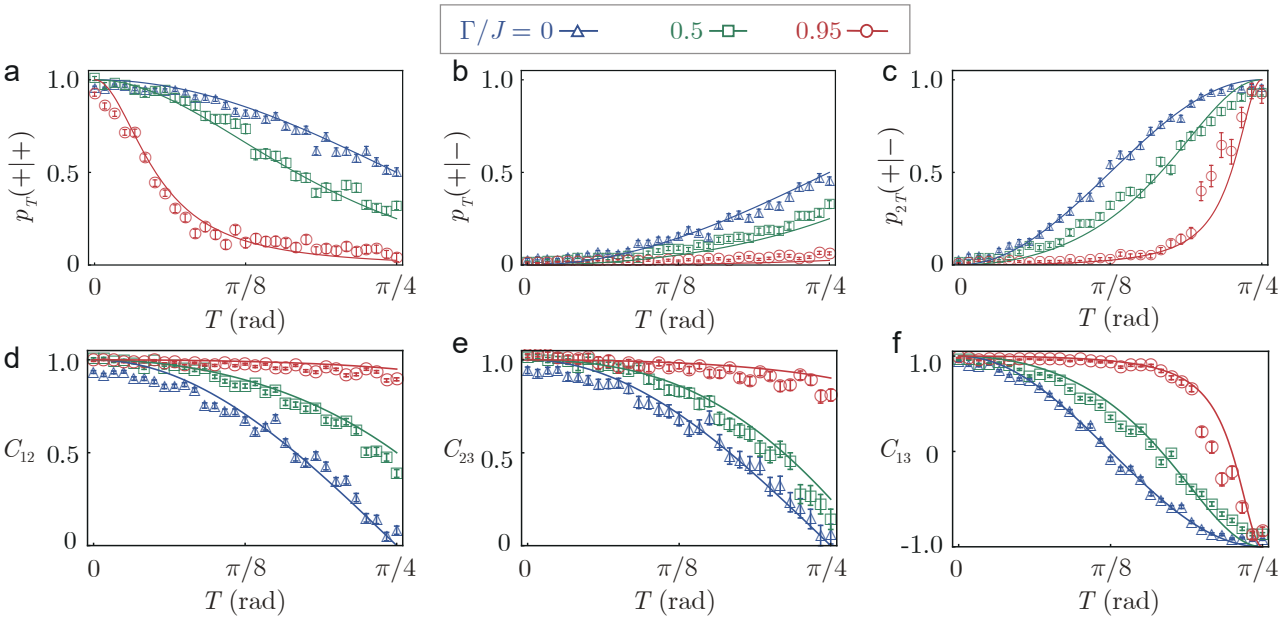

FIG. S.2. (a-c) Measurement results of the conditional probabilities $p_T(+|+)$ (a), $p_T(+|-)$ (b), and $p_{2T}(+|-)$ (c) versus the measurement time interval T for $\Gamma/J = 0$, 0.5 and 0.95. (d-f) Correlation functions C_{12} (d), C_{23} (e), and C_{13} (f) versus the measurement time interval T for $\Gamma/J = 0$, 0.5 and 0.95.

then applying the evolution operation $U(\alpha, \tau = \pi/4)$, and finally measuring the normalized population $p^n_{y+} = \frac{\langle\hat{\sigma}_y\rangle+1}{2}$, where we have chosen $Q = 1$. However, obtaining the probability

$$p'(Q) = \sum_{Q_0=\pm1} p(Q|Q_0)p(Q_0) \tag{S.5}$$

with an earlier measurement applied to the initial state requires several different measurement processes. The probability $p(Q_0 = +1)$ $[p(Q_0 = -1)]$ is obtained by measuring $p^n_{y+} = \frac{\langle\hat{\sigma}_y\rangle+1}{2}$ $(p^n_{y-} = \frac{1-\langle\hat{\sigma}_y\rangle}{2})$ right after the initial state $|\psi\rangle_0$ is prepared. The conditional probability $p(Q = 1|Q_0 = +1)$ $[p(Q = 1|Q_0 = -1)]$ requires the measurement of p^n_{y+} for the initial state $|+\rangle_y$ $(|-\rangle_y)$ followed by the unitary evolution operator $U(\alpha, \tau = \pi/4)$ given in Sec. B 1. Experimental results for $p(Q)$, $p(Q_0) = \pm1$, and $p(Q = 1|Q_0 = \pm1)$ are shown in Fig. S.3. The quantum witness W can be obtained using Eq. (7) in the main text.

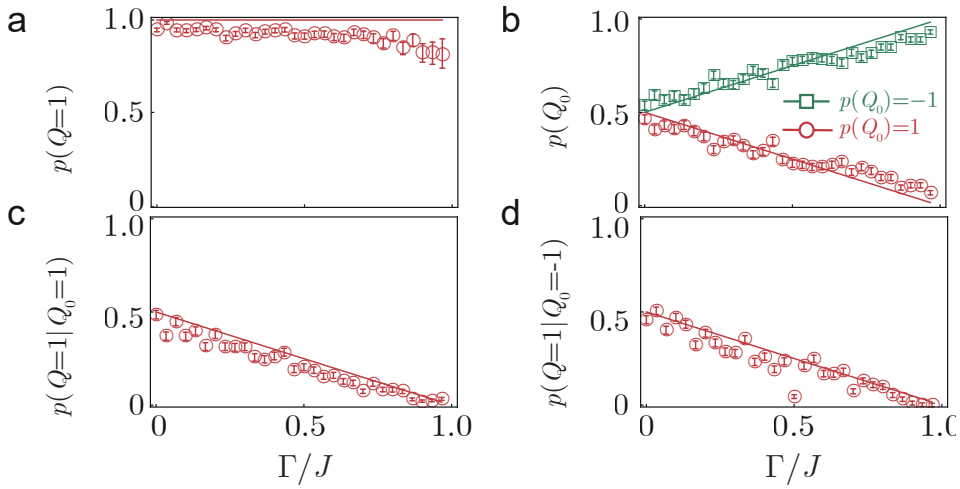

FIG. S.3. (a-d) Measurement results of the probabilities $p(Q = 1)$ (a), $p(Q_0 = \pm1)$ (b), $p(Q = 1|Q_0 = 1)$ (c), and $p(Q = 1|Q_0 = -1)$ (d) as a function of Γ/J.

E. Construction of the $\mathcal{PT}$-symmetric system

1. Theoretical construction of the unitary operator $U(\alpha,\tau)$

According to the theory in Ref. [3], a $\mathcal{PT}$-symmetric system can be reinterpreted as a subsystem of a Hermitian system with higher dimension. In our experiment, we use two 2-dimensional subsystems $\mathcal{H}_S$ and $\mathcal{H}_A$, which are expanded by $\{|1\rangle, |2\rangle\}$ and $\{|3\rangle, |4\rangle\}$ as shown in Fig. S.1(a), to construct a 4-dimensional Hilbert space $\mathcal{H}_S \oplus \mathcal{H}_A$. The unitary operator $U(\alpha,\tau)$ in Eq. (S.2) for the 4-dimensional space can be constructed by the Naimark dilation method as [3]

$$U = \begin{pmatrix} F & G \\ -G & F \end{pmatrix}, \tag{S.6}$$

where

$$F = \cos(\tau) I_2^m - \mathrm{i}\frac{\Omega}{J}\sin(\tau)\sigma_x^m, \tag{S.7}$$

$$G = \frac{\Gamma}{J}\sin(\tau)\sigma_z^m, \tag{S.8}$$

I_2^m denotes the 2-dimensional identity matrix, and $\sigma_{x,y,z}^m$ are the Pauli matrices.

2. Theoretical construction of the metric operator η

Based on the definition of the metric operator η, it should meet the condition

$$\eta \hat{H}_{\mathrm{PT}} - \hat{H}_{\mathrm{PT}}^{\dagger}\eta = 0, \tag{S.9}$$

where $\hat{H}_{\mathrm{PT}}^{\dagger}$ is the self-adjoint Hamiltonian of $\hat{H}_{\mathrm{PT}}$ in Eq. (2) of the main text. According to Refs. [3, 4], the metric operator can be easily constructed by taking advantage of the eigenvectors (labeled as $|E_+\rangle$ and $|E_-\rangle$) of $\hat{H}_{\mathrm{PT}}$ and has the form of $\eta = (\Psi\Psi^{\dagger})^{-1}$, where $\Psi = [|E_+\rangle, |E_-\rangle]$ is the constructed matrix by arranging the two eigenvectors as columns.

F. Theoretical derivation of the evolution speed and the correlation functions

1. Dynamics of the nonlinear von Neumann equation

Non-Hermitian systems have exhibited excellent ability of the acceleration of the quantum state evolution [5]. Such acceleration effect can be theoretically explored using the Bloch equations. Consider a two-level system governing by the $\mathcal{PT}$-symmetric Hamilton

$$\hat{H}_{\mathrm{PT}} = J\hat{\sigma}_x + \mathrm{i}\Gamma\hat{\sigma}_z, \tag{S.10}$$

where $J > \Gamma$ indicates the $\mathcal{PT}$-symmetric unbroken region. Starting from an initial state, the dynamics of the normalized density matrix $\hat{\rho}$ can be described by the following nonlinear von Neumann equation [6]

$$\dot{\hat{\rho}} = -\mathrm{i}J[\hat{\sigma}_x, \hat{\rho}] + \Gamma\{\hat{\sigma}_z, \hat{\rho}\} - 2\Gamma\hat{\rho}[\mathrm{Tr}(\hat{\sigma}_z\hat{\rho})]. \tag{S.11}$$

Express the density matrix $\hat{\rho}$ as $\hat{\rho} = (\hat{I} + \vec{r}\cdot\hat{\vec{\sigma}})/2$, where the Bloch vector $\vec{r} = (r_x, r_y, r_z) = (\langle\hat{\sigma}_x\rangle, \langle\hat{\sigma}_y\rangle, \langle\hat{\sigma}_z\rangle)$. Then based on Eq. (S.11), the Bloch equations can be derived as:

$$\begin{aligned} \dot{r}_x &= -2\Gamma r_x r_z, \\ \dot{r}_y &= -2(J r_z + \Gamma r_y r_z), \\ \dot{r}_z &= 2(J r_y - \Gamma r_z^2 + \Gamma). \end{aligned} \tag{S.12}$$

In the $\mathcal{PT}$-symmetric unbroken region, when the initial state is chosen as $|-\rangle_y$, the analytical solution for the above Bloch equations can be found as:

$$\begin{aligned} r_x &= 0, \\ r_y &= -\frac{\Gamma + J\cos(2\tau)}{J + \Gamma\cos(2\tau)}, \\ r_z &= -\frac{\sqrt{J-\Gamma}\sqrt{J+\Gamma}\sin(2\tau)}{J + \Gamma\cos(2\tau)}, \end{aligned} \tag{S.13}$$

where $\tau = t\sqrt{J^2 - \Gamma^2}$ is the scaled time. And when the initial state is $|+\rangle_y$, the analytical solution has the form of:

$$\begin{aligned} r_x &= 0, \\ r_y &= \frac{\Gamma - J\cos(2\tau)}{-J + \Gamma\cos(2\tau)}, \\ r_z &= \frac{\sqrt{J-\Gamma}\sqrt{J+\Gamma}\sin(2\tau)}{J - \Gamma\cos(2\tau)}. \end{aligned} \tag{S.14}$$

The dynamics of the Bloch vector described by Eq. (S.13) manifests the acceleration effect of the $\mathcal{PT}$-symmetric qubit as shown in Fig. 3.

G. Evolution speed of the $\mathcal{PT}$-symmetric qubit

For two pure qubit states $|\psi\rangle$ and $|\phi\rangle$, the Fubini-Study metric is defined as

$$s = \arccos(|\langle\psi|\phi\rangle|). \tag{S.15}$$

When preparing the initial state in $|-\rangle_y$, the normalized quantum state governed by the $\mathcal{PT}$-symmetric Hamiltonian $\hat{H}_{\mathrm{PT}}$ can be written as

$$|\psi(\tau)\rangle = -\frac{\sqrt{J-\Gamma}\sin(\tau)}{\sqrt{J+\Gamma\cos(2\tau)}}|+\rangle_y + \frac{\sqrt{J+\Gamma}\cos(\tau)}{\sqrt{J+\Gamma\cos(2\tau)}}|-\rangle_y . \tag{S.16}$$

Using $s = \arccos(|\langle\psi(\tau)|-\rangle_y|)$, the evolution speed can be derived as

$$v = \frac{\mathrm{d}s}{\mathrm{d}\tau} = \frac{\left|J^2 - \Gamma^2\right|}{\left|\sqrt{J^2-\Gamma^2}(J + \Gamma\cos(2\tau))\right|}. \tag{S.17}$$

In the experiment, the obtained states usually are mixed. In this case, the Fubini-Study metric for two density matrices ρ_1 and ρ_2 are computed as

$$s = \arccos\left(\mathrm{Tr}\sqrt{\sqrt{\rho_1}\rho_2\sqrt{\rho_1}}\right), \tag{S.18}$$

as shown in Fig. 3d of the main text.

1. *Analytical forms of the correlation functions*

Using the results of Eqs. (S.13) and (S.14), the analytical forms for the conditional probabilities in Sec. C can be expressed as:

$$\begin{aligned}
p_{_T}(+|+) &= \frac{(J-\Gamma)\cos^2(\tau)}{J-\Gamma\cos(2\tau)},\\
p_{_T}(-|+) &= \frac{(J+\Gamma)\sin^2(\tau)}{J-\Gamma\cos(2\tau)},\\
p_{_T}(+|-) &= \frac{(J-\Gamma)\sin^2(\tau)}{J+\Gamma\cos(2\tau)},\\
p_{_T}(-|-) &= \frac{(J+\Gamma)\cos^2(\tau)}{J+\Gamma\cos(2\tau)},\\
p_{_{2T}}(+|-) &= \frac{(J-\Gamma)\sin^2(2\tau)}{J+\Gamma\cos(4\tau)},\\
p_{_{2T}}(-|-) &= \frac{(J+\Gamma)\cos^2(2\tau)}{J+\Gamma\cos(4\tau)}.
\end{aligned} \tag{S.19}$$

Then the two-time correlation functions can be obtained as

$$\begin{aligned}
C_{12} &= -p_{_T}(+|-)+p_{_T}(-|-) = \frac{\Gamma+J\cos(2\tau)}{J+\Gamma\cos(2\tau)},\\
C_{13} &= -p_{_{2T}}(+|-)+p_{_{2T}}(-|-) = \frac{\Gamma+J\cos(4\tau)}{J+\Gamma\cos(4\tau)},\\
C_{23} &= p_{_T}(+|-)p_{_T}(+|+)-p_{_T}(+|-)p_{_T}(-|+)-p_{_T}(-|-)p_{_T}(+|-)+p_{_T}(-|-)p_{_T}(-|-)\\
&= \frac{J\Gamma^2+\cos(2\tau)\Big\{J(J^2+J\Gamma-\Gamma^2)-\Gamma\cos(2\tau)\big[-J^2+J\Gamma+\Gamma^2+J^2\cos(2\tau)\big]\Big\}}{\big[J-\Gamma\cos(2\tau)\big]\big[J+\Gamma\cos(2\tau)\big]^2}.
\end{aligned} \tag{S.20}$$

Finally, the Leggett-Garg parameter is computed as

$$K_3 = C_{12}+C_{23}-C_{13}. \tag{S.21}$$

The results of Eq. (S.20) apply to the $\mathcal{PT}$-symmetric unbroken region. In the broken region, by solving the Bloch equations Eq. (S.12), under the condition of $J \leqslant \Gamma$, we can obtain the analytical two-time correlation functions as:

$$\begin{aligned}
C_{12} &= \frac{\Gamma+J\cosh(2\tau)}{J+\Gamma\cosh(2\tau)},\\
C_{13} &= \frac{\Gamma+J\cosh(4\tau)}{J+\Gamma\cosh(4\tau)},\\
C_{23} &= \frac{J\Gamma^2+\cosh(2\tau)\Big\{J(J^2+J\Gamma-\Gamma^2)-\Gamma\cosh(2\tau)\big[-J^2+J\Gamma+\Gamma^2+J^2\cosh(2\tau)\big]\Big\}}{\big[J-\Gamma\cosh(2\tau)\big]\big[J+\Gamma\cosh(2\tau)\big]^2}.
\end{aligned} \tag{S.22}$$

The maximal temporal quantum correlation in our model can be found by numerically maximizing K_3 when varying the measurement interval τ in both the $\mathcal{PT}$-symmetric unbroken and broken regions, as shown in Fig. 4e of the main text.

Besides the above results, based on Eqs. (S.13) and (S.14), we can also derive the analytical form of the quantum witness in the unbroken region,

$$W = \frac{J+\Gamma}{2J}, \tag{S.23}$$

which is shown in Fig. 4f of the main text.

[1] J. Zhang, M. C. Zhang, Y. Xie, C. W. Wu, B. Q. Ou, T. Chen, W. S. Bao, P. Haljan, W. Wu, S. Zhang and P. X. Chen, Parallel electromagnetically induced transparency near ground-state cooling of a trapped-ion crystal, Phys. Rev. Appl. **18**, 014022 (2022).

[2] M. A. Nielsen and I. L. Chuang, *Quantum Computation and Quantum Information, 10th anniversary ed* (Cambridge University Press, Cambridge, 2010), pp. 189-191.

[3] U. Günther and B. F. Samsonov, Naimark-dilated $\mathcal{PT}$-symmetric brachistochrone, Phys. Rev. Lett. **101**, 230404 (2008).

[4] C. M. Bender, D. C. Brody, and H. F. Jones, Scalar quantum field theory with a complex cubic interaction, Phys. Rev. Lett. **93**, 251601 (2004).

[5] C. M. Bender, D. C. Brody, H. F. Jones and B. K. Meister, Faster than Hermitian quantum mechanics, Phys. Rev. Lett. **98**, 040403 (2007).

[6] D. C. Brody and E. M. Graefe, Mixed-state evolution in the presence of gain and loss, Phys. Rev. Lett. **109**, 230405 (2012).